RESfM: Robust Deep Equivariant Structure from Motion

Fadi Khatib[1]* **Yoni Kasten**[2] **Dror Moran**[1] **Meirav Galun**[1] **Ronen Basri**[1]
[1]Weizmann Institute of Science [2]NVIDIA

Abstract

Multiview Structure from Motion is a fundamental and challenging computer vision problem. A recent deep-based approach utilized matrix equivariant architectures for simultaneous recovery of camera pose and 3D scene structure from large image collections. That work, however, made the unrealistic assumption that the point tracks given as input are almost clean of outliers. Here, we propose an architecture suited to dealing with outliers by adding a multiview inlier/outlier classification module that respects the model equivariance and by utilizing a robust bundle adjustment step. Experiments demonstrate that our method can be applied successfully in realistic settings that include large image collections and point tracks extracted with common heuristics that include many outliers, achieving state-of-the-art accuracies in almost all runs, superior to existing deep-based methods and on-par with leading classical (non-deep) sequential and global methods.

1 Introduction

Simultaneous recovery of camera pose and 3D structure from large image collections, commonly termed Multiview Structure from Motion (SfM), is a longstanding fundamental problem in computer vision with applications in augmented and virtual reality, robot manipulation, and more. Classical, as well as some recent deep-based SfM techniques, rely on extracting point tracks, i.e., point matches across multiple frames, to solve for camera poses and structure. However, existing heuristics for point track extraction and chaining often return erroneous (*outlier*) point matches due to significant viewpoint, illumination differences, and repetitive scene structures, adversely affecting the performance of SfM methods. Designing robust methods that can effectively overcome the effect of such outliers, therefore, has been an active thread of research in the past several decades.

A promising approach to SfM is based on generalizations of *projective factorization*. This approach uses the observation that if we stack the tracked points in a matrix, which we denote by M, and assuming M has no missing entries and is error-free, then there exists a set of scale factors such that scaling each tracked point in M will make it rank 4. Enforcing this constraint allows us to recover both the 3D positions of the points that generate the tracks and the poses of the observing cameras (Sturm & Triggs, 1996). However, prior algorithms required M to be complete and error-free; they were sensitive to initialization and were applied only in uncalibrated settings, producing a reconstruction up to a global projective ambiguity.

A deep network architecture for projective factorization was recently proposed in (Moran et al., 2021). Their network uses a sets-of-sets architecture (Hartford et al., 2018), which is permutation equivariant to both the rows and columns of the point track matrix. Brynte et al. (2023) proposed a related architecture that uses self-attention blocks to improve runtime further. Both these networks showed promising results on image collections acquired with a single camera. However, as we show in this paper (see also Figure 1), they fail to handle collections of internet photos, primarily because they were not designed to remove outlier matches.

In this paper, we aim to construct a robust network for projective factorization that can handle outliers in realistic settings. To this end, we return to (Moran et al., 2021)'s architecture and enrich it with an outlier removal module. Our module is integrated into the equivariant architecture, allowing it to identify outliers if their motion is inconsistent with other points in the same image or if their motion is

*The project page: https://robust-equivariant-sfm.github.io/

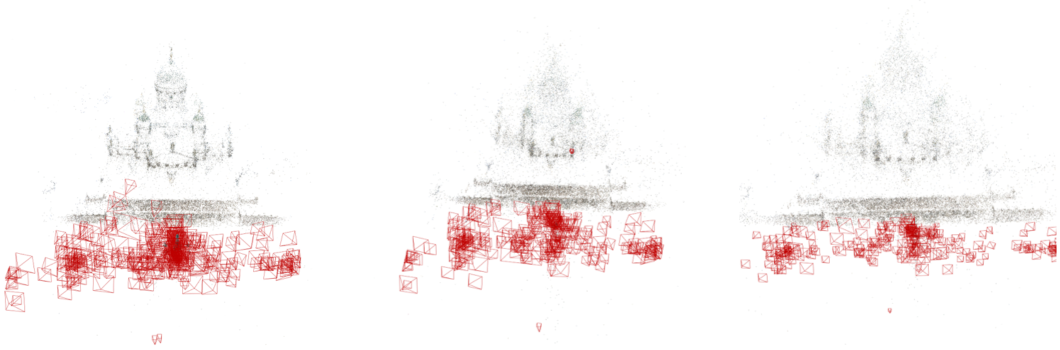

(a) Our recovery (b) ESFM recovery (c) GASFM recovery

Figure 1: **3D reconstruction and camera pose recovery in the presence of outliers.** The figure shows reconstruction results (point clouds) and camera poses (in red) obtained with our method (left) and existing deep-based methods including ESFM (Moran et al., 2021) (middle), and GASFM (Brynte et al., 2023) for scene 0185 (MegaDepth dataset, 30% outliers). It is evident that our method copes well with outliers in contrast to these existing methods.

at odds with the motion of other points in their track. We train this module with a cross-entropy loss, using labels that are inferred automatically using COLMAP reconstructions, allowing for cross-scene generalization. We further utilize a final bundle adjustment (BA) step that is robust to classification errors. Experiments show that our network improves over the methods of Moran et al. (2021); Brynte et al. (2023) in almost all runs, obtaining state-of-the-art accuracies and runtimes comparable to the leading classical methods, including COLMAP, Theia, and GLOMAP (Schönberger & Frahm, 2016; Sweeney et al., 2015; Pan et al., 2024).

In summary, our contributions are:

1. A deep network for *robust* multiview SfM, utilizing a sets-of-sets permutation equivariant architecture.
2. A trainable architecture allows for cross-scene and cross-dataset generalization.
3. Our method is applied to large collections (hundreds of images) of uncontrolled internet photos. This, to the best of our knowledge, is the first deep method for simultaneous recovery of structure and camera pose that handles such challenging inputs.
4. Our method achieves highly accurate recovery of camera pose and structure, superior to existing deep methods and on par both in accuracy and speed with state-of-the-art classical methods.
5. A benchmark with point tracks and pseudo ground truth computed with COLMAP on the MegaDepth and 1DSFM datasets.

2 Related Work

The recovery of camera pose and 3D structure from image collections has been a central subject of research in computer vision in the past several decades, leading to multiple breakthroughs that enabled accurate reconstructions from hundreds and even thousands of unordered images (Agarwal et al., 2011; Schönberger & Frahm, 2016; Snavely et al., 2006; Wu, 2013). In the typical *sequential pipeline* point tracks are first extracted from the input images. Camera pose and 3D structure are next computed for two images and then updated by processing the remaining images one by one. This pipeline yields highly accurate recovery of pose and structure but can be slow when applied to large image collections. Alternative global approaches attempt to compute camera poses by a process of "averaging" the relative rotations and translations estimated from pairwise essential matrices (Martinec & Pajdla, 2007; Özyeşil et al., 2017; Kasten et al., 2019). The recent Theia (Sweeney et al., 2015) and GLOMAP (Pan et al., 2024), in particular, were shown to yield accurate recovery. Related to our approach is the projective factorization (PF) method (Sturm & Triggs, 1996; Dai et al., 2010; Lin et al., 2017), which is based on the observation that the full track matrix is derived from a rank four matrix by a per-point scale factor. Classical PF algorithms, however, are limited to uncalibrated settings and address neither missing entries nor outliers.

Recent deep-learning techniques attempt to improve these pipelines by exploiting priors over the input images, camera settings, and 3D structures learned with these networks. Existing methods attempt to improve keypoint detection and matching (Lindenberger et al., 2021; Sun et al., 2021; DeTone et al., 2018; Lindenberger et al., 2023; Sarlin et al., 2020), produce point tracks (He et al., 2023), formulate differentiable alternatives to RANSAC (Yi et al., 2018; Zhang et al., 2019; Zhao et al., 2021; Sun et al., 2020), or directly infer the relative orientation and location for pairs of images (Khatib et al., 2024; Laskar et al., 2017; Cai et al., 2021; Rockwell et al., 2022; Arnold et al., 2022).

Recent work proposed end-to-end methods for camera pose estimation. Works such as RelPose (Zhang et al., 2022) and its successor, RelPose++ (Lin et al., 2023), harness energy-based models to recover camera poses from inputs that include the relative rotations between images. Similarly, SparsePose (Sinha et al., 2023) learns to regress initial camera poses which are then refined iteratively. PoseDiffusion (Wang et al., 2023b) employs a diffusion model to refine camera poses. Zhang et al. (2024) improves on this by focusing on purifying the camera rays. These works, however, are only applied to small collections of images (typically $\leq$30) and are commonly applied in object-centric scenarios, e.g., as in (Reizenstein et al., 2021). Recent learnable SfM pipelines such as VGGSfM (Wang et al., 2023a), DUST3R (Wang et al., 2023c), and MAST3R (Leroy et al., 2024) are still limited to handling only a small number of images, while Ace-Zero (Brachmann et al., 2024) and FlowMap (Smith et al., 2024) are applicable to video sequences with constant illumination.

Motivated by projective factorization schemes Moran et al. (2021) presented a trainable network for simultaneous camera pose and 3D structure recovery. Arranging the input point tracks in a matrix, an equivariant network to row and column permutations, i.e., sets-of-sets architecture, is used to regress the camera poses and the 3D point cloud coordinates. The network is trained with unsupervised data by optimizing a reprojection loss and is applied at inference to novel scenes not seen in training. Additional fine-tuning and Bundle Adjustment (BA) are applied to attain sub-pixel reprojection errors. This approach achieved highly accurate pose and structure recovery on large image collections (with several hundreds of images) of outdoor urban scenes. However, it has a significant limitation as it requires the point tracks matrix, to be almost free of outliers. This greatly restricts its applicability in realistic settings.

GASFM (Brynte et al., 2023) replaces the set-of-sets architecture in (Moran et al., 2021) with a graph attention network for increased expressiveness, enabling them to avoid fine-tuning, thereby reducing inference runtime compared to (Moran et al., 2021) without compromising the performance. Chen et al. (2024) applies (Moran et al., 2021)'s network (with some modifications) to aerial images captured with GPS information under roughly constant camera orientation. Neither Brynte et al. (2023) nor Chen et al. (2024) demonstrate results on point tracks contaminated by a significant portion of outliers.

Our approach extends and improves over the work of Moran et al. (2021) by integrating a multiview inlier/outlier classification module that respects and exploits the equivariant structure of the network and by introducing a robust BA scheme. This allows us to work with realistic point tracks contaminated with outliers obtained with standard heuristics and still achieve high-accuracy performance.

3 METHOD

3.1 PROBLEM FORMULATION

We assume a stationary scene viewed by m cameras with unknown poses. We obtain as input a (sparse) point track tensor M that includes 2D observations of n 3D points viewed by partial sets of cameras. We further assume in this work that the cameras are internally calibrated. A camera matrix therefore is expressed in the form of $P_i = [R_i|\mathbf{t}_i]$, where $R_i \in SO(3)$ is a rotation matrix. With this notation, the camera is placed at the position $-R_i^T\mathbf{t}_i$. We denote by $\mathbf{X}_j \in \mathbb{R}^3$ the j'th 3D scene point and by $\mathbf{x}_{ij} \in \mathbb{R}^2$ its observed position in the i^{th} image. The set $T_j = \{\mathbf{x}_{i_1j}, \mathbf{x}_{i_2j}, ...\}$ with $C_j = \{i_1, i_2, ...\} \subseteq [m]$ represents the j'th track, associated with the j'th 3D point. These tracks are generally constructed in a preprocessing step by employing heuristics and, therefore, are contaminated by small displacement errors (noisy measurements) and outliers.

We arrange the tracks $T_1, \ldots, T_n$ in the columns of the measurement point track tensor M. The tensor M is of size $m \times n \times 2$, so the rows of M correspond to the m cameras, and its columns correspond

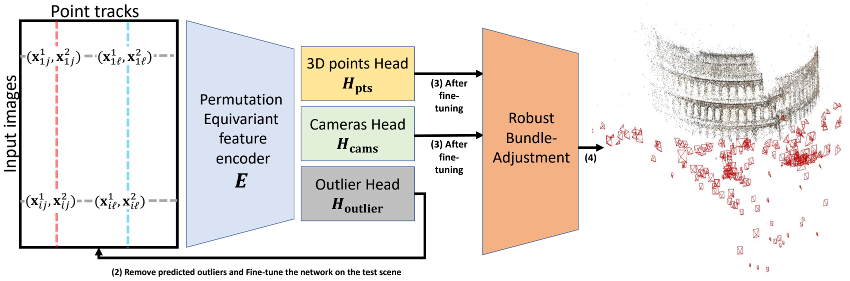
Point tracks
Input images
$(\mathbf{x}^1_{1j}, \mathbf{x}^2_{1j})$
$(\mathbf{x}^1_{1\ell}, \mathbf{x}^2_{1\ell})$
$(\mathbf{x}^1_{ij}, \mathbf{x}^2_{ij})$
$(\mathbf{x}^1_{i\ell}, \mathbf{x}^2_{i\ell})$
Permutation Equivariant feature encoder
$\boldsymbol{E}$
3D points Head
$\boldsymbol{H}_{\mathbf{pts}}$
Cameras Head
$\boldsymbol{H}_{\mathbf{cams}}$
Outlier Head
$\boldsymbol{H}_{\mathbf{outlier}}$
(3) After fine-tuning
(3) After fine-tuning
Robust Bundle-Adjustment
(4)
(2) Remove predicted outliers and Fine-tune the network on the test scene

Figure 2: **Network architecture**. Our network comprises four main steps: (1) Given a point track tensor (left), an equivariant feature encoder module (light blue) produces a latent feature representation. (2) The outlier head (gray) applies an inlier/outlier classification. Predicted outliers are then removed from the input track, and the encoder is fine-tuned for 1000 epochs. (3) 3D point locations and camera poses are predicted by the point head (yellow) and the camera head (green), respectively. (4) The predicted camera poses and the point cloud are finally optimized by robust bundle adjustment (orange).

to the unknown 3D points whose contaminated projections are given. We set $(M_{ij1}, M_{ij2}) \doteq \mathbf{x}_{ij}$ if $i \in C_j$ and otherwise leave M_{ij1} and M_{ij2} empty.

We aim to recover the pose parameters of the m camera matrices and the 3D positions of the n feature points. Additionally, we seek to classify each track point as either an inlier or an outlier. The output of our network will comprise three matrices: $P \in \mathbb{R}^{m\times 7}$ for the set of cameras matrices, $X \in \mathbb{R}^{n\times 3}$ for the 3D structure, and $O \in \mathbb{R}^{m\times n}$ for the track point classification results. We represent camera pose by a rotation quaternion $\mathbf{q}_i \in \mathbb{R}^4$ and a translation vector $\mathbf{t}_i \in \mathbb{R}^3$. Classification results in O are represented by scores in $[0, 1]$, where $\mathbf{x}_{ij}$ with $O_{ij} \geq 0.6$ is considered an outlier. (The threshold 0.6 was determined by a hyperparameter search.) Note that we classify individual points as outliers, while other points in the same track may be classified as inliers.

3.2 Network Architecture

We use an architecture that is equivariant to row and column permutations of the tensor M, equivalent respectively to independent permutations of the cameras and the 3D points. It comprises four modules: a permutation equivariant feature encoder, followed by an inlier/outlier classification module, pose, and structure regression modules (see Fig. 2).

Permutation equivariant feature encoder. This module takes as input the tensor $M \in \mathbb{R}^{m\times n\times 2}$ and outputs a latent representation in $\mathbb{R}^{m\times n\times d}$, where $d = 256$. It comprises three permutation equivariant layers with linear maps interspersed with pointwise non-linear ReLU function. A linear equivariant map is the core of permutation equivariant networks. In our case, permutation equivariance should apply to the rows (cameras) and columns (3D points) of the tensor M. Hartford et al. (2018) showed that the space of linear maps that keep the permutation equivariant property of a single channel (i.e., the input and the output are matrices) is spanned by the identity, the row sums, the column sums, and the matrix sum. This can be applied to multiple input and output channels from a feature space with d channels $\mathbb{R}^{m\times n\times d}$ to a feature space with d' channels $\mathbb{R}^{m\times n\times d'}$ in the following way:

$$L(\tilde{M})_{ij} = W_1 \tilde{M}_{ij} + W_2 \sum_{k=1}^{m} \tilde{M}_{kj} + W_3 \sum_{l=1}^{n} \tilde{M}_{il} + W_4 \sum_{k=1}^{m}\sum_{l=1}^{n} \tilde{M}_{kl} + \mathbf{b}, \tag{1}$$

where $\tilde{M}_{ij} \in \mathbb{R}^d$ represents the vector of entries of $\tilde{M}$ at the (i, j) position, $W_i \in \mathbb{R}^{d'\times d}$ for $i = 1, ..., 4$, and $\mathbf{b} \in \mathbb{R}^{d'}$ are learnable parameters. We follow Moran et al. (2021) and replace sums by averages over the non-empty entries of M, yielding invariance to the number of observed projections.

Inlier/Outlier classification module. Given the latent representation $\mathbb{R}^{m\times n\times d}$ provided by the equivariant feature encoder, this module, H_{outlier}, employs three MLP layers followed by a sigmoid function. The output is a matrix $O \in [0, 1]^{m\times n}$ expressing the probability of each entry being an outlier. Note that this module respects the equivariance property, allowing our model to classify track points based on their relations to other points of the same track as well as other points within the same image.

Pose and structure regression modules. Utilizing the latent representation $\mathbb{R}^{m \times n \times d}$ from the equivariant feature encoder, the pose and structure heads, H_{cams} and H_{pts}, consist of three MLP layers each. The first head, H_{cams}, processes the pooled average of the features along the columns $\mathbb{R}^{m \times d}$, where each camera's features are encoded into a vector in $\mathbb{R}^d$, and outputs a tensor in $\mathbb{R}^{m \times 7}$. This tensor encapsulates the camera's translation vector (first three values) and orientation (last four values, represented as a quaternion), collectively forming the camera's projection matrix. The second head, H_{pts}, processes the pooled average of features along the rows $\mathbb{R}^{n \times d}$, where each scene point is encoded by a vector in $\mathbb{R}^d$, and outputs a tensor in $\mathbb{R}^{n \times 3}$, representing the coordinates of the scene points.

3.3 Loss Function

Our loss function combines two terms

$$\mathcal{L} = \mathcal{L}_{\text{outliers}} + \alpha \mathcal{L}_{\text{reprojection}} \tag{2}$$

where the hyperparameter $\alpha = 10$ balances the two terms and was determined by a hyperparameter search. The outlier classification loss, $\mathcal{L}_{\text{outliers}}$, employs a Binary Cross-Entropy (BCE) loss. The second part of the loss $\mathcal{L}_{\text{reprojection}}$ is an unsupervised objective, and it includes reprojection and hinge loss terms. The reprojection loss aims to minimize the error between projected scene points and their detected positions in the image, similar to the objective in bundle adjustment. A hinge loss is also used to prevent the prediction of non-positive depth values, thus ensuring a physically plausible scene reconstruction.

$$\mathcal{L}_{\text{reprojection}} = \frac{1}{p} \sum_{i=1}^{m} \sum_{j=1}^{n} \xi_{ij} s_{ij}, \tag{3}$$

where $p = \sum_{j=1}^{n} |T_j|$ the number of measured projections, and $\xi_{ij} \in \{0, 1\}$ is indicating whether point $\mathbf{X}_j$ is detected in image I_i.

$$s_{ij} = \begin{cases} r_{ij}, & P_i^3 \mathbf{X}_j \geq h \\ h_{ij}, & P_i^3 \mathbf{X}_j < h, \end{cases}$$

and

$$r_{ij} = \left\| \left(\mathbf{x}_{ij}^1 - \frac{P_i^1 \mathbf{X}_j}{P_i^3 \mathbf{X}_j}, \mathbf{x}_{ij}^2 - \frac{P_i^2 \mathbf{X}_j}{P_i^3 \mathbf{X}_j} \right) \right\|,$$

and $h_{ij} = \max(0, h - P_i^3 \mathbf{X}_j)$, where $h > 0$ is a small constant (in our setting, $h = 0.0001$). h_{ij} therefore is the hinge loss for the depth value of $\mathbf{X}_j$ in image I_i.

3.4 Training

During training, we processed all training scenes sequentially for each epoch. For each scene, we randomly selected a subset of 10%-20% of the images. We employed a validation set for early stopping, selecting the checkpoint with minimal error. More details can be found in Appendix A.

3.5 Inference

After training our network, we test the network on *unseen scenes*. We first apply inlier/outlier classification predictions to remove outliers, and then fine-tune the network for the tested scene. This yields predictions for camera poses and 3D point locations. Having those predictions, we apply our robust Bundle Adjustment procedure.

Fine-tuning. At this step, we leverage our inlier/outlier classification prediction and remove the points predicted as outliers from the point tracks tensor M (using the threshold 0.6). Subsequently, similar to (Moran et al., 2021), we fine-tune the network for the tested scene by minimizing the unsupervised reprojection loss equation 3 for 1000 epochs.

Robust Bundle Adjustment. As common in SfM pipelines, a post-processing step of applying bundle adjustment is necessary to achieve sub-pixel reconstruction accuracy. Standard BA was found to be ineffective as it was unable to handle the remaining outliers. We therefore utilize a Robust Bundle Adjustment process:

1. Apply bundle adjustment (BA) to the predicted cameras and predicted 3D points.
2. Remove 3D points with projection error higher than 5 pixels and remove 3D points viewed in fewer than 3 cameras.
3. If the view graph of the point tracks becomes unconnected due to the removals, then we take the largest component and discard point tracks that originate from the removed images.
4. Triangulate the remaining point tracks and apply a second round of (standard) BA.

More details on the robust BA stage can be found in Appendix A.

4 Experiments

4.1 Datasets

Our network is trained on scenes from the MegaDepth dataset (Li & Snavely, 2018). It is then tested on both novel scenes from the MegaDepth dataset and in cross-dataset generalization tests on the 1DSfM dataset (Wilson & Snavely, 2014), Strecha (Strecha et al., 2008), and BlendedMVS (Yao et al., 2020). These datasets offer a diverse range of real-world scenes, which are instrumental in assessing the robustness and versatility of our proposed architecture across different environments and challenges.

The point tracks, which our network takes as input, are constructed by concatenating pairwise matches between images within each scene. These matches are obtained by applying RANSAC to SIFT matches, ensuring a robust selection of correspondences by mitigating the influence of outliers. The detailed procedure for constructing these point tracks, including parameter settings and algorithmic choices, is provided in Appendix C.

MegaDepth (Li & Snavely, 2018). The MegaDepth dataset comprises 196 different outdoor scenes, each populated with internet photos showcasing popular landmarks around the globe. To facilitate a comprehensive evaluation, we divide the dataset into two groups based on the number of images per scene: (1) scenes with fewer than 1000 images, and (2) scenes with more than 1000 images. From the first group, we randomly sampled 27 scenes to serve as our training dataset, along with four scenes designated for validation purposes. For the test set, we randomly selected 14 scenes from the first group. Moreover, from each scene in the second group, we randomly sampled 300 images to represent a condensed version of the scene. These samples form a part of the test dataset, introducing a significant challenge for Structure from Motion (SfM) methods due to the reduced number of images representing vast and complex scenes. In Table 1, the scenes above the middle rule belong to Group 1 of scenes with fewer than 1000 images, while the scenes below the rule belong to Group 2.

1DSFM (Wilson & Snavely, 2014). The 1DSFM dataset is renowned for its collection of diverse scenes reconstructed from community photo collections. It includes a variety of urban locations, making it a valuable resource for evaluating Structure from Motion (SfM) and multi-view stereo algorithms. For our purposes, the dataset offers a challenging yet realistic setting to evaluate our architecture's effectiveness in dealing with large-scale reconstructions. Specifically, we train the models on MegaDepth dataset and assess its generalization to 1DSFM dataset.

Strecha (Strecha et al., 2008). The Strecha dataset is widely used for benchmarking 3D reconstruction algorithms and consists of five outdoor scenes. It provides high-resolution images alongside ground-truth data acquired with a LIDAR system. However, each scene includes only a small ($\leq$ 30) number of images acquired with a single camera. We perform our tests on four of these scenes.

BlendedMVS (Yao et al., 2020). The BlendedMVS is a synthetic dataset built by reconstructing textured meshes and rendering them into color images and depth maps, which are blended with the original inputs to create realistic data, thereby generating ground truth for camera poses.

Ground truth camera poses. Challenging datasets such as MegaDepth and 1DSFM lack ground truth. Therefore, as is common in the field Jiang et al. (2013); Wilson & Snavely (2014); Cui & Tan (2015); Ozyesil & Singer (2015); Brynte et al. (2023); Wang et al. (2023a); Zhang et al. (2024), we utilize COLMAP, a state-of-the-art incremental Structure from Motion (SfM) method, to establish ground truth camera poses for the scenes in those datasets. COLMAP stands as one of the most popular solutions in the field due to its robust performance in reconstructing 3D models from unordered image collections. We apply COLMAP directly to the scene images to obtain the ground truth poses. Additionally, we show results with the smaller datasets Strecha (Strecha et al., 2008) and BlendedMVS (Yao et al., 2020) for which ground truth camera poses are available.

4.2 Baselines

ESFM (Moran et al., 2021). We compare our method to this equivariant SfM method where, for fairness, we replace BA with our robust BA. The model is trained on MegaDepth dataset and evaluated both on MegaDepth and 1DSFM. We conduct two distinct evaluations: one in which ESFM is trained and tested on the original point tracks, which include outliers (denoted as ESFM), and another evaluation where the model is trained and tested on the same point tracks, but in which outliers have been removed (this version is denoted as ESFM*). By testing ESFM on the original contaminated tracks, we evaluate the method's ability to handle realistic settings. A comparison with outlier-free tracks provides an empirical upper bound for our method.

GASFM (Brynte et al., 2023). We compare our method to GASFM, which replaces the set-of-sets architecture in ESFM (Moran et al., 2021) with a graph attention network. This modification increases expressiveness, enabling them to avoid fine-tuning and thereby reduce inference runtime compared to the traditional SfM method (Schönberger & Frahm, 2016), without compromising performance when tested on the outlier-free Olsson's dataset (Olsson & Enqvist, 2011). We trained and tested GASFM on the original MegaDepth point tracks (which include outliers) and also tested it on the 1DSFM dataset scenes.

To allow a fair comparison, in both ESFM and GASFM, the inference step is followed by 1000 epochs of fine-tuning.

VGGSfM (Wang et al., 2024) is a differentiable, end-to-end trainable SfM pipeline, simplifying some of its components to streamline the process while maintaining accurate 3D reconstruction capabilities.

MASt3R (Leroy et al., 2024) is a pipeline for SfM that merges pairwise pointmap predictions through an optimization-based global alignment procedure to handle image collections effectively.

Theia (Sweeney et al., 2015). A widely recognized global SfM pipeline that begins by estimating camera rotations using rotation averaging, followed by translation averaging to estimate camera positions. It concludes with global triangulation to reconstruct the 3D point cloud and a final bundle adjustment, similar to other global SfM techniques.

GLOMAP (Pan et al., 2024). GLOMAP is a newly proposed global SfM pipeline that addresses the limitations of previous global methods, which were considered efficient but less robust than incremental approaches. Instead of relying on separate translation averaging and point triangulation, GLOMAP combines them into a single global positioning step, optimizing both camera positions and 3D structure simultaneously.

4.3 Metrics and Evaluation

We evaluate our results using camera position and orientation errors. Specifically, after performing a similarity alignment per scene, we compare our camera orientation predictions with the ground truth ones by measuring angular differences in degrees. Similarly, we measure differences between our predicted and ground truth camera locations. For a fair comparison, both our method and all the baseline methods (except VGGSfM, which is applied directly to the input images) were run with the same set of point tracks. For all methods, we apply a final post-processing step of our robust bundle adjustment. When highlighting the best results in the tables, we do not compare to ESFM*.

Table 1: **MegaDepth experiment.** For each scene, we show the number of input images (denoted N_c) and the fraction of outliers. For each model, we show the number of images used for reconstruction (denoted N_r) and mean values of the rotation (in degrees) and translation errors. (Above the middle rule are Group 1 scenes with <1000 images; below are Group 2 scenes with >1000 images, subsampled to 300 for testing.) Winning results are marked in bold and underlined. Yellow represents the best result among the deep-based algorithms and green among the classical algorithms.

Scene	N_c	Outliers%	**Ours**			ESFM			GASFM			Theia			GLOMAP			ESFM*		
			N_r	Rot	Trans	N_r	Rot	Trans	N_r	Rot	Trans	N_r	Rot	Trans	N_r	Rot	Trans	N_r	Rot	Trans
0238	522	44.6	283	2.61	**0.325**	76	11.49	1.088	76	9.89	0.969	**506**	1.21	0.334	499	**0.74**	0.349	512	3.06	0.142
0060	528	41.6	503	0.29	**0.029**	303	14.92	2.167	258	18.48	2.736	**525**	0.85	0.124	522	**0.11**	0.048	524	0.02	0.005
0197	870	40.7	667	4.22	0.333	281	9.62	0.980	454	12.23	1.678	**855**	1.16	0.227	814	**0.43**	**0.129**	825	0.41	0.050
0094	763	40.1	537	3.77	0.750	93	14.91	1.772	359	2.27	0.322	**742**	**0.75**	**0.160**	717	0.88	3.907	643	4.55	1.018
0265	571	38.8	346	**1.25**	**0.389**	270	22.14	2.712	274	22.29	2.756	554	5.83	2.216	**558**	7.46	2.839	559	0.12	0.039
0083	635	31.3	596	0.64	0.058	568	4.40	0.558	574	3.95	0.245	**632**	0.37	0.372	614	**0.08**	**0.016**	556	21.02	1.904
0076	558	30.5	524	0.37	0.094	454	3.86	0.655	431	**0.11**	**0.015**	**549**	0.78	0.120	541	0.17	0.042	547	0.04	0.006
0185	368	30.0	350	**0.06**	**0.010**	261	1.76	0.271	254	1.36	0.184	**365**	0.41	0.094	**365**	0.16	0.051	130	38.49	2.478
0048	512	24.2	474	4.69	0.178	469	4.03	0.235	481	1.44	**0.073**	**507**	0.41	0.105	506	**0.15**	0.224	508	0.09	0.006
0024	356	23.0	309	2.03	0.398	271	9.08	1.320	300	9.80	2.546	**355**	0.56	0.219	339	**0.15**	**0.104**	343	2.78	0.568
0223	214	17.0	204	3.76	0.510	191	11.97	2.272	194	13.69	2.649	212	3.34	0.519	**214**	**1.75**	**0.275**	211	0.09	0.017
5016	28	0.2	**28**	0.12	0.016	**28**	0.09	**0.015**	**28**	0.09	**0.015**	**28**	0.10	0.061	**28**	**0.08**	0.046	28	0.04	0.009
0046	440	14.6	399	0.95	0.043	97	1.68	0.082	426	0.45	0.019	434	0.25	0.112	**440**	**0.03**	**0.007**	33	37.09	1.387
0099	299	47.4	190	3.53	0.709	104	4.17	0.862	128	8.13	1.116	**297**	3.28	0.664	255	**0.15**	**0.085**	243	6.22	1.075
1001	285	43.9	251	**1.70**	**0.661**	241	4.40	1.846	261	3.26	1.143	276	7.97	4.014	**281**	4.56	3.817	280	0.12	0.085
0231	296	42.2	246	0.84	**0.065**	214	0.85	0.080	209	0.91	0.088	**286**	1.37	0.322	279	**0.73**	0.134	284	0.56	0.022
0411	299	29.9	273	**0.13**	**0.020**	188	15.89	1.650	232	2.95	0.304	**293**	0.39	0.196	269	0.19	0.148	288	0.08	0.013
0377	295	27.5	210	0.29	0.018	162	0.54	0.044	167	**0.13**	**0.013**	**269**	1.13	0.205	268	0.65	0.237	279	1.19	0.147
0102	299	25.8	284	0.28	**0.059**	255	1.55	0.403	278	1.79	0.478	**294**	2.31	0.698	293	**0.15**	0.101	155	21.00	3.470
0147	298	24.6	207	**4.62**	**0.325**	197	4.90	0.522	225	10.89	0.961	284	6.36	0.934	**290**	6.75	3.542	251	3.22	0.215
0148	287	24.6	197	**0.60**	**0.035**	206	1.64	0.133	209	1.73	0.135	275	13.98	1.558	**283**	22.73	2.646	249	0.94	0.083
0446	298	22.1	288	0.72	**0.046**	283	2.02	0.193	291	1.71	0.237	289	1.23	0.391	**296**	**0.20**	0.071	294	0.92	0.115
0022	297	21.2	274	0.29	**0.039**	241	1.38	0.184	263	0.54	0.082	**296**	0.58	0.160	281	**0.22**	0.087	289	0.30	0.646
0327	298	21.0	271	0.26	0.090	281	1.83	0.398	284	**0.25**	**0.029**	288	1.27	0.360	**290**	15.54	2.035	294	0.06	0.008
0015	284	20.6	215	1.04	0.167	142	5.00	0.920	149	14.02	2.105	244	2.21	0.389	**274**	**0.28**	**0.095**	185	4.51	0.941
0455	298	19.8	293	0.68	0.105	293	0.68	0.138	294	0.74	0.144	294	0.77	0.159	**298**	**0.35**	**0.064**	298	0.89	0.109
0496	297	19.2	281	**0.35**	**0.055**	281	3.59	0.311	277	0.68	0.061	285	1.40	0.550	**291**	0.44	0.303	293	0.29	0.028
1589	299	17.4	290	0.14	**0.019**	284	0.92	0.131	283	2.71	0.505	288	0.82	0.193	**299**	**0.07**	0.041	296	0.40	0.053
0012	299	16.3	287	**0.40**	**0.027**	291	5.20	0.327	294	0.88	0.114	129	1.04	0.318	**295**	0.51	0.121	294	0.47	0.044
0104	284	16.2	193	**0.29**	**0.029**	220	24.40	2.174	228	4.10	0.306	265	17.05	1.530	**280**	19.69	0.834	200	0.78	0.044
0019	299	15.4	250	**0.06**	**0.008**	267	9.34	0.329	293	2.34	0.113	271	0.81	0.250	**296**	0.09	0.025	296	4.90	0.180
0063	293	14.5	262	0.46	0.048	262	2.15	0.456	257	0.44	**0.040**	268	0.92	0.605	**288**	**0.32**	0.100	275	0.32	0.301
0130	285	14.4	192	**0.20**	**0.023**	192	1.46	0.058	194	2.27	0.070	187	1.20	0.349	**281**	2.00	0.909	282	1.59	0.179
0080	284	12.9	139	**0.59**	**0.096**	137	1.34	0.325	139	2.18	0.104	278	2.62	0.868	**283**	1.92	0.237	163	1.92	0.173
0240	298	11.9	275	3.13	0.265	274	1.69	0.170	272	2.54	0.227	278	1.31	0.470	**294**	**0.39**	**0.135**	296	0.27	0.111
0007	290	11.7	172	0.91	0.041	260	38.74	2.284	280	1.87	0.101	277	1.24	0.174	**290**	**0.19**	**0.035**	286	1.59	0.264
Mean	379	25.6	298	**1.29**	**0.169**	239	6.77	0.780	267	4.53	0.630	346	2.42	0.556	353	2.51	0.662	319	4.45	0.443

4.4 Results

Our results for the MegaDepth and 1DSFM test scenes are shown in Tables 1 and 2, respectively. Each table lists the number of input images (N_c), the fraction of outlier track points, and our results compared to the baseline methods. For each method, we provide the number of registered cameras (N_r) and mean camera orientation and position errors. It can be seen that our method outperforms both ESFM and GASFM in almost all runs, achieving accurate results that are close to what is obtained with ESFM on clean tracks (ESFM*). Our results are also on par with state-of-the-art classical methods, including Theia and GLOMAP, often yielding superior translation recovery (but handling fewer images). This demonstrates the utility of our method in realistic settings.

We further tested our method on the smaller Strecha and BlendedMVS datasets which include ground truth measurements. Our method is more accurate than the deep-based VGGSfM and MASt3R (that cannot run on the larger datasets) and is on par with the classical methods, see Tables 3 and 4.

Qualitative results. Figure 1 shows an example of 3D reconstructions and camera parameters obtained using our method compared to those obtained with ESFM and GASFM. These results clearly demonstrate that our method produces superior 3D reconstructions, effectively handling outliers in contrast to the other baselines. Additional qualitative results are provided in Appendix A.

Runtime and resources. Table 5 compares the runtimes of our method with the classical COLMAP, Theia, and GLOMAP when applied to the point tracks generated in our preprocessing stage. Our approach is significantly faster than COLMAP and GLOMAP but is slower than Theia. We note that

Table 2: **1DSFM experiment.** For each scene, we show the number of input images (denoted N_c) and the fraction of outliers. For each model, we show the number of images used for reconstruction (denoted N_r) and mean values of the rotation (in degrees) and translation errors. Winning results are marked in bold and underlined. Yellow represents the best result among the deep-based algorithms and green among the classical algorithms.

Scene	N_c	Outliers%	**Ours**			ESFM			GASFM			Theia			GLOMAP			ESFM*		
			N_r	Rot	Trans	N_r	Rot	Trans	N_r	Rot	Trans	N_r	Rot	Trans	N_r	Rot	Trans	N_r	Rot	Trans
Alamo	573	32.6	484	3.66	0.515	457	4.53	**0.319**	448	5.85	0.460	553	4.42	1.433	**557**	**2.45**	1.520	526	3.17	0.321
Ellis Island	227	25.1	214	0.82	**0.122**	196	21.13	2.053	198	21.91	2.081	213	5.01	1.527	**219**	**0.58**	0.155	220	0.38	0.033
Madrid Metropolis	333	39.4	244	8.42	0.827	151	19.56	1.946	159	21.97	2.205	-	-	-	**320**	**1.22**	**0.242**	290	25.25	2.664
Montreal Notre Dame	448	31.7	346	2.82	0.352	309	10.13	1.773	311	11.77	1.557	422	4.47	1.285	**444**	**0.60**	**0.211**	414	0.16	0.020
Notre Dame	549	35.6	517	**1.2**	**0.231**	487	1.95	0.226	499	1.74	0.232	314	3.70	0.828	**543**	2.73	0.389	528	0.72	0.051
NYC Library	330	33.6	224	3.96	0.429	177	4.42	0.468	218	7.65	0.667	**534**	4.06	1.141	323	**0.58**	**0.189**	301	2.62	0.226
Piazza del Popolo	336	33.1	249	2.20	**0.186**	204	10.77	0.997	198	9.05	1.063	325	3.31	1.053	**331**	**0.80**	0.188	303	4.31	0.604
Tower of London	467	27.0	94	**0.67**	**0.026**	196	22.02	2.239	152	32.36	2.306	448	6.61	1.189	**466**	0.81	0.138	213	13.08	0.704
Vienna Cathedral	824	31.4	479	**1.52**	**0.112**	551	6.52	0.537	558	7.98	0.573	772	12.25	1.663	**822**	2.00	2.414	536	1.51	0.069
Yorkminster	432	29.0	331	14.54	1.468	215	10.63	0.637	251	13.01	0.846	390	8.35	1.916	**418**	**0.95**	**0.316**	389	12.63	0.994

Table 3: **Strecha experiment.** For each scene, we present the number of input images (denoted N_c) and the fraction of outliers. For each model, we show the number of images used for reconstruction (denoted N_r) and the mean values of the rotation error (in degrees), translation error (in meters) and runtime (in seconds). The best results are marked in bold and the second best are underlined.

Scene	N_c	Out.%	**Ours**				MASt3R				VGGSfM				Theia				COLMAP				GLOMAP			
			N_r	Rot	Trans	Time	N_r	Rot	Trans	Time	N_r	Rot	Trans	Time	N_r	Rot	Trans	Time	N_r	Rot	Trans	Time	N_r	Rot	Trans	Time
entry-P10	10	4.8	10	0.024	0.008	3.3	10	0.442	0.055	19	10	0.165	0.056	10.3	10	0.024	0.008	**0.9**	10	**0.023**	**0.007**	36.0	10	0.187	0.026	12.5
fountain-P11	11	1.4	11	0.028	0.003	5.3	11	0.160	0.026	22	11	0.172	0.016	15.4	11	**0.027**	**0.002**	**1.5**	11	**0.027**	0.003	37.0	11	0.194	0.022	38.6
Herz-Jesus-P8	8	1.8	8	0.026	**0.004**	2.6	8	0.363	0.037	16	8	0.206	0.042	8.7	8	**0.025**	0.005	**0.6**	8	0.026	**0.004**	22.0	8	0.091	0.015	5.0
Herz-Jesus-P25	25	2.8	24	0.030	**0.006**	9.4	25	0.869	0.057	81	25	0.158	0.046	19.6	25	**0.026**	**0.006**	**2.4**	25	0.028	**0.006**	60.0	25	0.138	0.013	76.6
Mean	1.5	2.7	13.5	0.027	**0.005**	5.2	13.5	0.459	0.044	34.5	13.5	0.175	0.040	13.5	13.5	**0.026**	**0.005**	**1.4**	13.5	**0.026**	**0.005**	38.8	13.5	0.153	0.019	33.2

Table 4: **BlendedMVS experiment.** For each scene, we present the number of input images (denoted N_c) and the fraction of outliers. For each model, we show the number of images used for reconstruction (denoted N_r) and the mean values of the rotation error (in degrees), translation error, and runtime (in seconds). The best results are marked in bold and the second best are underlined.

Scene	N_c	Out.%	**Ours**				MASt3R				VGGSfM				Theia				COLMAP				GLOMAP			
			N_r	Rot	Trans	Time	N_r	Rot	Trans	Time	N_r	Rot	Trans	Time	N_r	Rot	Trans	Time	N_r	Rot	Trans	Time	N_r	Rot	Trans	Time
scene0	75	2.0	75	0.016	0.0007	54	75	0.501	0.191	516	75	0.045	0.0106	61	75	0.009	0.0017	**49**	75	**0.006**	**0.0005**	106	75	0.007	0.0016	198
scene1	51	1.4	51	0.011	0.0021	32	51	0.919	0.173	1017	51	0.098	0.0112	32	51	0.029	0.0099	**18**	51	**0.007**	**0.0003**	67	51	0.024	0.0102	117
scene2	33	2.2	33	0.009	0.0006	21	33	1.972	0.130	117	33	0.227	0.0180	30	33	0.045	0.0098	**15**	33	**0.003**	**0.0002**	55	33	0.025	0.0060	87
scene3	66	8.8	66	0.007	0.0007	52	66	0.927	0.045	815	66	0.372	0.0174	52	66	0.019	0.0018	**21**	66	**0.004**	**0.0002**	128	66	0.008	0.0017	392

the fine-tuning phase is the most time-consuming part of our pipeline. Table 6 further compares the utilization of resources of the deep-based methods. Our method utilizes slightly more parameters than (Moran et al., 2021) and is two orders of magnitude smaller than (Brynte et al., 2023). In terms of memory usage and proceeding speed our method is the most efficient.

Classification performance. Table 7 (left) presents various classification metrics to assess the performance of our inlier/outlier classification module. After removing the predicted outliers, our method significantly decreases the percentage of outliers in the point tracks. These classification results enable the robust BA module to perform well and produce accurate reconstruction and camera pose estimation, yielding another significant decrease in the outlier ratio. Removing these remaining outliers is challenging since these outlier matches survived the RANSAC preprocessing.

4.5 Ablations

For ablations, we first examine the impact of our permutation sets-of-sets equivariant architecture. We replace our inlier/outlier classifier module with a set equivariant PointNet architecture. The input in this experiment consists of a set of quadruples, (x, y, c, t), where (x, y) are the keypoint coordinates, c represents camera id, and t denotes track id. As shown in Table 7, our equivariant architecture achieves superior classification accuracies, justifying the importance of using sets-of-sets equivariance.

Next, we examine the importance of the equivariant features. We compare our method, which is trained end-to-end, to (1) the case that only the classification head is trained while the feature encoder is frozen (i.e., trained as in ESFM without outlier classification), and (2) the same architecture but

Table 5: **Runtime.** Given the same contaminated point tracks, we compare the runtime of our proposed method to classical methods, including COLMAP, Theia, and GLOMAP.

Scene	N_c	Outliers%	**Ours**						COLMAP			Theia			GLOMAP		
			Inference (Secs)	Fine-tuning (Secs)	BA (Secs)	Total (Mins)	N_r	$N_r/t \uparrow$	Total (Mins)	N_r	$N_r/t \uparrow$	Total (Mins)	N_r	$N_r/t \uparrow$	Total (Mins)	N_r	$N_r/t \uparrow$
Alamo	573	32.6	0.004	674.3	355.6	17.2	484	28.2	83.7	568	6.8	13.4	553	**41.4**	40.0	557	13.9
Ellis Island	227	25.1	0.004	103.4	66.1	2.8	214	75.9	14.9	223	15.0	1.1	213	**201.8**	7.7	219	28.6
Madrid Metropolis	333	39.4	0.003	286.8	61.2	5.8	244	42.1	25.1	323	12.9	-	-	-	7.1	320	**45.2**
Montreal Notre Dame	448	31.7	0.005	190.62	174.9	6.1	346	56.7	35.9	447	12.5	3.7	422	**114.6**	13.5	444	32.9
Notre Dame	549	35.6	0.003	1101.75	229.4	22.2	517	23.3	72.6	546	7.5	11.6	534	**46.0**	21.1	543	25.8
NYC Library	330	33.6	0.004	153.15	88.0	4.0	224	55.7	26.6	330	12.4	1.5	314	**204.2**	7.3	323	44.5
Piazza del Popolo	336	33.1	0.002	91.6	70.0	2.7	249	92.6	9.6	334	34.9	3.0	325	**108.8**	5.9	331	56.0
Tower of London	467	27.0	0.003	271.65	84.0	5.9	94	15.9	65.0	467	7.2	3.1	448	**142.5**	23.5	466	19.8
Vienna Cathedral	824	31.4	0.005	470.35	963.5	23.9	479	20.0	98.9	824	8.3	11.2	772	**68.8**	41.6	822	19.8
Yorkminster	432	29.0	0.002	270	192.5	7.7	331	42.9	31.4	419	13.3	2.9	390	**135.3**	14.8	418	28.2

Table 6: **Resources.** Performance comparison between different methods in terms of a number of parameters, maximum memory usage, and processing speed (images per minute) averaged over the 1dsfm scenes.

Method	**Ours**	ESFM	GASFM
#Params (millions) ↓	0.73	**0.66**	145.17
Max Memory (GBs) ↓	**9.5**	10.1	25.7
Image/minutes ↑	**45.3**	40.9	10.7

with the classification head removed (equivalent ESFM). It can be seen in Table 8 that training the feature encoder in an end-to-end schedule makes a crucial impact on the accuracy of our method.

Finally, in Appendix D, we validate the importance of our Robust BA; we compare it to a standard BA, showing that the accuracy is significantly improved with our Robust BA.

Table 7: **Classification metric and architecture ablation.** Inlier/outlier classification accuracies and the fraction of outliers predicted with our permutation-equivariant network (sets of sets) compared to an alternative set network (PointNet architecture).

Scene	N_c	Outliers%	**Ours**						**PointNet architecture**				
		Outliers% Input	Recall (inliers)	Recall (outliers)	Precision (outliers)	F-score (outliers)	Outliers% Predicted ↓	Outliers% Robust BA ↓	Recall (inliers)	Recall (outliers)	Precision (outliers)	F-score (outliers)	Outliers% Predicted ↓
Alamo	573	32.6	**65.8**	**74.3**	**51.5**	**60.8**	**16.0**	**10.8**	36.4	**74.3**	36.3	48.8	25.7
Ellis Island	227	25.1	**61.9**	70.4	**38.4**	**49.7**	**13.9**	**5.7**	31.1	**70.8**	25.8	37.8	24.0
Madrid Metropolis	333	39.4	**62.6**	62.3	**51.7**	**56.5**	**27.9**	**30.0**	36.2	**71.6**	41.9	52.9	33.6
Montreal Notre Dame	448	31.7	**61.5**	70.4	**46.4**	**56.0**	**18.6**	**10.8**	33.8	**71.6**	33.9	46.0	28.5
Notre Dame	549	35.6	**62.8**	61.4	**48.5**	**54.2**	**26.0**	**17.7**	33.8	**71.0**	35.7	47.5	30.8
NYC Library	330	33.6	**51.7**	**81.1**	**46.5**	**59.1**	**15.9**	**9.2**	33.7	68.0	37.0	47.9	35.2
Piazza del Popolo	336	33.1	**56.7**	**78.1**	**47.5**	**59.0**	**16.3**	**7.5**	26.1	81.1	35.5	49.4	26.6
Tower of London	467	27.0	**28.3**	**85.4**	**30.3**	**44.8**	**15.9**	**2.9**	42.5	59.0	27.3	37.3	26.1
Vienna Cathedral	824	31.4	**58.5**	**65.8**	**42.2**	**51.5**	**21.2**	**13.6**	38.3	64.9	32.6	43.4	29.7
Yorkminster	432	29.0	**50.6**	**71.8**	**37.5**	**49.3**	**18.7**	**10.2**	48.7	53	29.9	38.2	28.5
Mean	451.9	31.9	**56.0**	**72.1**	**44.1**	**54.1**	**19.0**	**11.8**	36.1	68.5	33.6	44.9	28.9

Table 8: **Encoder ablation.** For each scene, we show the number of input images (denoted N_c) and the fraction of outliers. For each model, we show the number of images used for reconstruction (denoted N_r) and the mean values of the rotation (in degrees) and translation errors.

Scene	N_c	Outliers%	**Ours**			Frozen Encoder			No Encoder (ESFM)		
			N_r	Rot	Trans	N_r	Rot	Trans	N_r	Rot	Trans
Alamo	573	32.6	484	**3.66**	0.515	**511**	3.79	0.394	457	4.53	**0.338**
Ellis Island	227	25.1	**214**	**0.82**	**0.122**	198	20.60	2.094	196	21.13	2.091
Madrid Metropolis	333	39.4	**244**	**8.42**	0.827	231	9.09	**0.794**	151	19.56	1.932
Montreal Notre Dame	448	31.7	**346**	2.82	0.352	335	**1.17**	**0.244**	309	10.13	1.778
Notre Dame	549	35.6	517	1.2	0.231	**518**	**0.69**	**0.168**	487	1.95	0.233
NYC Library	330	33.6	224	**3.96**	**0.429**	**232**	4.07	0.542	177	4.42	0.546
Piazza del Popolo	336	33.1	249	**2.20**	**0.186**	**254**	5.59	0.739	204	10.77	1.006
Tower of London	467	27.0	94	**0.67**	**0.026**	141	25.93	1.601	**196**	22.02	2.226
Vienna Cathedral	824	31.4	479	**1.52**	**0.112**	523	2.94	0.222	**551**	6.52	0.553
Yorkminster	432	29.0	331	14.54	1.468	**354**	13.24	1.183	215	**10.63**	**0.636**

5 CONCLUSION

We present a permutation equivariant architecture for robust multiview structure from motion. By integrating a sets-of-sets equivariant inlier/outlier classification module, our proposed method copes well with point-track tensors contaminated with many outliers originating from scenes that include hundreds of images. In addition, we modified the bundle adjustment module to make it robust enough to handle classification errors. Our method successfully handles challenging datasets that include hundreds of uncontrolled internet images, achieving highly accurate recovery, superior to existing deep methods and on par with state-of-the-art classical methods. However, we observed cases in which our method uses only a subset of the input cameras. This occurs due to an excess removal of predicted outliers, which might yield an unconnected viewing graph. We plan to address this limitation in our future work.

Acknowledgments

This research was supported in part by the Israel Science Foundation, grant No. 1639/19, by the Israeli Council for Higher Education (CHE) via the Weizmann Data Science Research Center, by the MBZUAI-WIS Joint Program for Artificial Intelligence Research and by research grants from the Estates of Bernice Bernath and Marni Josephs Grossman; Joel B. Levey; Tully and Michele Plesser and the Anita James Rosen and Harry Schutzman Foundations.

References

Sameer Agarwal, Keir Mierle, and Others. Ceres solver. `http://ceres-solver.org`.

Sameer Agarwal, Yasutaka Furukawa, Noah Snavely, Ian Simon, Brian Curless, Steven M Seitz, and Richard Szeliski. Building rome in a day. *Communications of the ACM*, 54(10):105–112, 2011.

Eduardo Arnold, Jamie Wynn, Sara Vicente, Guillermo Garcia-Hernando, Áron Monszpart, Victor Adrian Prisacariu, Daniyar Turmukhambetov, and Eric Brachmann. Map-free visual relocalization: Metric pose relative to a single image. In *ECCV*, 2022.

Eric Brachmann, Jamie Wynn, Shuai Chen, Tommaso Cavallari, Áron Monszpart, Daniyar Turmukhambetov, and Victor Adrian Prisacariu. Scene coordinate reconstruction: Posing of image collections via incremental learning of a relocalizer. *arXiv preprint arXiv:2404.14351*, 2024.

Lucas Brynte, José Pedro Iglesias, Carl Olsson, and Fredrik Kahl. Learning structure-from-motion with graph attention networks. *arXiv preprint arXiv:2308.15984*, 2023.

Ruojin Cai, Bharath Hariharan, Noah Snavely, and Hadar Averbuch-Elor. Extreme rotation estimation using dense correlation volumes. In *Proceedings of the IEEE/CVF Conference on Computer Vision and Pattern Recognition*, pp. 14566–14575, 2021.

Zequan Chen, Jianping Li, Qusheng Li, Bisheng Yang, and Zhen Dong. Deepaat: Deep automated aerial triangulation for fast uav-based mapping, 2024.

Zhaopeng Cui and Ping Tan. Global structure-from-motion by similarity averaging. In *Proceedings of the IEEE International Conference on Computer Vision*, pp. 864–872, 2015.

Yuchao Dai, Hongdong li, and Mingyi He. Element-wise factorization for n-view projective reconstruction. pp. 396–409, 09 2010. ISBN 978-3-642-15560-4. doi: 10.1007/978-3-642-15561-1_29.

Daniel DeTone, Tomasz Malisiewicz, and Andrew Rabinovich. Superpoint: Self-supervised interest point detection and description. In *Proceedings of the IEEE conference on computer vision and pattern recognition workshops*, pp. 224–236, 2018.

Martin A Fischler and Robert C Bolles. Random sample consensus: a paradigm for model fitting with applications to image analysis and automated cartography. *Communications of the ACM*, 24 (6):381–395, 1981.

Jason Hartford, Devon Graham, Kevin Leyton-Brown, and Siamak Ravanbakhsh. Deep models of interactions across sets. In *International Conference on Machine Learning*, pp. 1909–1918. PMLR, 2018.

Xingyi He, Jiaming Sun, Yifan Wang, Sida Peng, Qixing Huang, Hujun Bao, and Xiaowei Zhou. Detector-free structure from motion. *arXiv preprint arXiv:2306.15669*, 2023.

Nianjuan Jiang, Zhaopeng Cui, and Ping Tan. A global linear method for camera pose registration. In *Proceedings of the IEEE international conference on computer vision*, pp. 481–488, 2013.

Yoni Kasten, Amnon Geifman, Meirav Galun, and Ronen Basri. Algebraic characterization of essential matrices and their averaging in multiview settings. In *Proceedings of the IEEE/CVF International Conference on Computer Vision*, pp. 5895–5903, 2019.

Fadi Khatib, Yuval Margalit, Meirav Galun, and Ronen Basri. Leveraging image matching toward end-to-end relative camera pose regression. *arXiv preprint arXiv:2211.14950*, 2024.

Diederik P Kingma and Jimmy Ba. Adam: A method for stochastic optimization. *arXiv preprint arXiv:1412.6980*, 2014.

Zakaria Laskar, Iaroslav Melekhov, Surya Kalia, and Juho Kannala. Camera relocalization by computing pairwise relative poses using convolutional neural network. In *Proceedings of the IEEE International Conference on Computer Vision Workshops*, pp. 929–938, 2017.

Vincent Leroy, Yohann Cabon, and Jérôme Revaud. Grounding image matching in 3d with mast3r. *arXiv preprint arXiv:2406.09756*, 2024.

Zhengqi Li and Noah Snavely. Megadepth: Learning single-view depth prediction from internet photos. In *Proceedings of the IEEE conference on computer vision and pattern recognition*, pp. 2041–2050, 2018.

Amy Lin, Jason Y Zhang, Deva Ramanan, and Shubham Tulsiani. Relpose++: Recovering 6d poses from sparse-view observations. *arXiv preprint arXiv:2305.04926*, 2023.

Yang Lin, Li Yang, Zhouchen Lin, Tong Lin, and Hongbin Zha. Factorization for projective and metric reconstruction via truncated nuclear norm. In *2017 International Joint Conference on Neural Networks (IJCNN)*, pp. 470–477, 2017. doi: 10.1109/IJCNN.2017.7965891.

Philipp Lindenberger, Paul-Edouard Sarlin, Viktor Larsson, and Marc Pollefeys. Pixel-perfect structure-from-motion with featuremetric refinement. In *Proceedings of the IEEE/CVF international conference on computer vision*, pp. 5987–5997, 2021.

Philipp Lindenberger, Paul-Edouard Sarlin, and Marc Pollefeys. LightGlue: Local Feature Matching at Light Speed. In *ICCV*, 2023.

David G Lowe. Distinctive image features from scale-invariant keypoints. *International journal of computer vision*, 60(2):91–110, 2004.

Daniel Martinec and Tomas Pajdla. Robust rotation and translation estimation in multiview reconstruction. In *2007 IEEE Conference on Computer Vision and Pattern Recognition*, pp. 1–8. IEEE, 2007.

Dror Moran, Hodaya Koslowsky, Yoni Kasten, Haggai Maron, Meirav Galun, and Ronen Basri. Deep permutation equivariant structure from motion. In *Proceedings of the IEEE/CVF International Conference on Computer Vision*, pp. 5976–5986, 2021.

Carl Olsson and Olof Enqvist. Stable structure from motion for unordered image collections. In *Image Analysis: 17th Scandinavian Conference, SCIA 2011, Ystad, Sweden, May 2011. Proceedings 17*, pp. 524–535. Springer, 2011.

Onur Ozyesil and Amit Singer. Robust camera location estimation by convex programming. In *Proceedings of the IEEE Conference on Computer Vision and Pattern Recognition*, pp. 2674–2683, 2015.

Onur Özyeşil, Vladislav Voroninski, Ronen Basri, and Amit Singer. A survey of structure from motion*. *Acta Numerica*, 26:305–364, 2017.

Linfei Pan, Dániel Baráth, Marc Pollefeys, and Johannes L Schönberger. Global structure-from-motion revisited. In *European Conference on Computer Vision (ECCV)*, 2024.

Adam Paszke, Sam Gross, Francisco Massa, Adam Lerer, James Bradbury, Gregory Chanan, Trevor Killeen, Zeming Lin, Natalia Gimelshein, Luca Antiga, et al. Pytorch: An imperative style, high-performance deep learning library. *Advances in neural information processing systems*, 32, 2019.

Jeremy Reizenstein, Roman Shapovalov, Philipp Henzler, Luca Sbordone, Patrick Labatut, and David Novotny. Common objects in 3d: Large-scale learning and evaluation of real-life 3d category reconstruction. In *Proceedings of the IEEE/CVF International Conference on Computer Vision*, pp. 10901–10911, 2021.

Chris Rockwell, Justin Johnson, and David F Fouhey. The 8-point algorithm as an inductive bias for relative pose prediction by ViTs. *arXiv preprint arXiv:2208.08988*, 2022.

Paul-Edouard Sarlin, Daniel DeTone, Tomasz Malisiewicz, and Andrew Rabinovich. SuperGlue: Learning feature matching with graph neural networks. In *CVPR*, 2020. URL `https://arxiv.org/abs/1911.11763`.

Johannes Lutz Schönberger and Jan-Michael Frahm. Structure-from-motion revisited. In *Conference on Computer Vision and Pattern Recognition (CVPR)*, 2016.

Samarth Sinha, Jason Y Zhang, Andrea Tagliasacchi, Igor Gilitschenski, and David B Lindell. Sparsepose: Sparse-view camera pose regression and refinement. In *Proceedings of the IEEE/CVF Conference on Computer Vision and Pattern Recognition*, pp. 21349–21359, 2023.

Cameron Smith, David Charatan, Ayush Tewari, and Vincent Sitzmann. Flowmap: High-quality camera poses, intrinsics, and depth via gradient descent. *arXiv preprint arXiv:2404.15259*, 2024.

Noah Snavely, Steven M Seitz, and Richard Szeliski. Photo tourism: exploring photo collections in 3d. In *ACM siggraph 2006 papers*, pp. 835–846. 2006.

Christoph Strecha, Wolfgang Von Hansen, Luc Van Gool, Pascal Fua, and Ulrich Thoennessen. On benchmarking camera calibration and multi-view stereo for high resolution imagery. In *2008 IEEE conference on computer vision and pattern recognition*, pp. 1–8. Ieee, 2008.

Peter Sturm and Bill Triggs. A factorization-based algorithm for multi-image projective structure and motion. In *European conference on computer vision*, pp. 709–720. Springer, 1996.

Jiaming Sun, Zehong Shen, Yuang Wang, Hujun Bao, and Xiaowei Zhou. LoFTR: Detector-free local feature matching with transformers. *CVPR*, 2021.

Weiwei Sun, Wei Jiang, Eduard Trulls, Andrea Tagliasacchi, and Kwang Moo Yi. Acne: Attentive context normalization for robust permutation-equivariant learning. In *Proceedings of the IEEE/CVF conference on computer vision and pattern recognition*, pp. 11286–11295, 2020.

Christopher Sweeney, Tobias Hollerer, and Matthew Turk. Theia: A fast and scalable structure-from-motion library. In *Proceedings of the 23rd ACM international conference on Multimedia*, pp. 693–696, 2015.

Jianyuan Wang, Nikita Karaev, Christian Rupprecht, and David Novotny. Visual geometry grounded deep structure from motion. *arXiv preprint arXiv:2312.04563*, 2023a.

Jianyuan Wang, Christian Rupprecht, and David Novotny. Posediffusion: Solving pose estimation via diffusion-aided bundle adjustment. In *Proceedings of the IEEE/CVF International Conference on Computer Vision*, pp. 9773–9783, 2023b.

Jianyuan Wang, Nikita Karaev, Christian Rupprecht, and David Novotny. Vggsfm: Visual geometry grounded deep structure from motion. In *Proceedings of the IEEE/CVF Conference on Computer Vision and Pattern Recognition*, pp. 21686–21697, 2024.

Shuzhe Wang, Vincent Leroy, Yohann Cabon, Boris Chidlovskii, and Jerome Revaud. Dust3r: Geometric 3d vision made easy. *arXiv preprint arXiv:2312.14132*, 2023c.

Kyle Wilson and Noah Snavely. Robust global translations with 1dsfm. In *Computer Vision–ECCV 2014: 13th European Conference, Zurich, Switzerland, September 6-12, 2014, Proceedings, Part III 13*, pp. 61–75. Springer, 2014.

Changchang Wu. Towards linear-time incremental structure from motion. In *2013 International Conference on 3D Vision-3DV 2013*, pp. 127–134. IEEE, 2013.

Yao Yao, Zixin Luo, Shiwei Li, Jingyang Zhang, Yufan Ren, Lei Zhou, Tian Fang, and Long Quan. Blendedmvs: A large-scale dataset for generalized multi-view stereo networks. In *Proceedings of the IEEE/CVF conference on computer vision and pattern recognition*, pp. 1790–1799, 2020.

Kwang Moo Yi, Eduard Trulls, Yuki Ono, Vincent Lepetit, Mathieu Salzmann, and Pascal Fua. Learning to find good correspondences. In *Proceedings of the IEEE conference on computer vision and pattern recognition*, pp. 2666–2674, 2018.

Jason Y Zhang, Deva Ramanan, and Shubham Tulsiani. Relpose: Predicting probabilistic relative rotation for single objects in the wild. In *European Conference on Computer Vision*, pp. 592–611. Springer, 2022.

Jason Y Zhang, Amy Lin, Moneish Kumar, Tzu-Hsuan Yang, Deva Ramanan, and Shubham Tulsiani. Cameras as rays: Pose estimation via ray diffusion. In *International Conference on Learning Representations (ICLR)*, 2024.

Jiahui Zhang, Dawei Sun, Zixin Luo, Anbang Yao, Lei Zhou, Tianwei Shen, Yurong Chen, Long Quan, and Hongen Liao. Learning two-view correspondences and geometry using order-aware network. In *Proceedings of the IEEE/CVF international conference on computer vision*, pp. 5845–5854, 2019.

Chen Zhao, Yixiao Ge, Feng Zhu, Rui Zhao, Hongsheng Li, and Mathieu Salzmann. Progressive correspondence pruning by consensus learning. In *Proceedings of the IEEE/CVF International Conference on Computer Vision*, pp. 6464–6473, 2021.

APPENDIX

A QUALITATIVE RESULTS

Figures 3 and 4 show reconstruction examples with our method, compared to other deep-based methods.

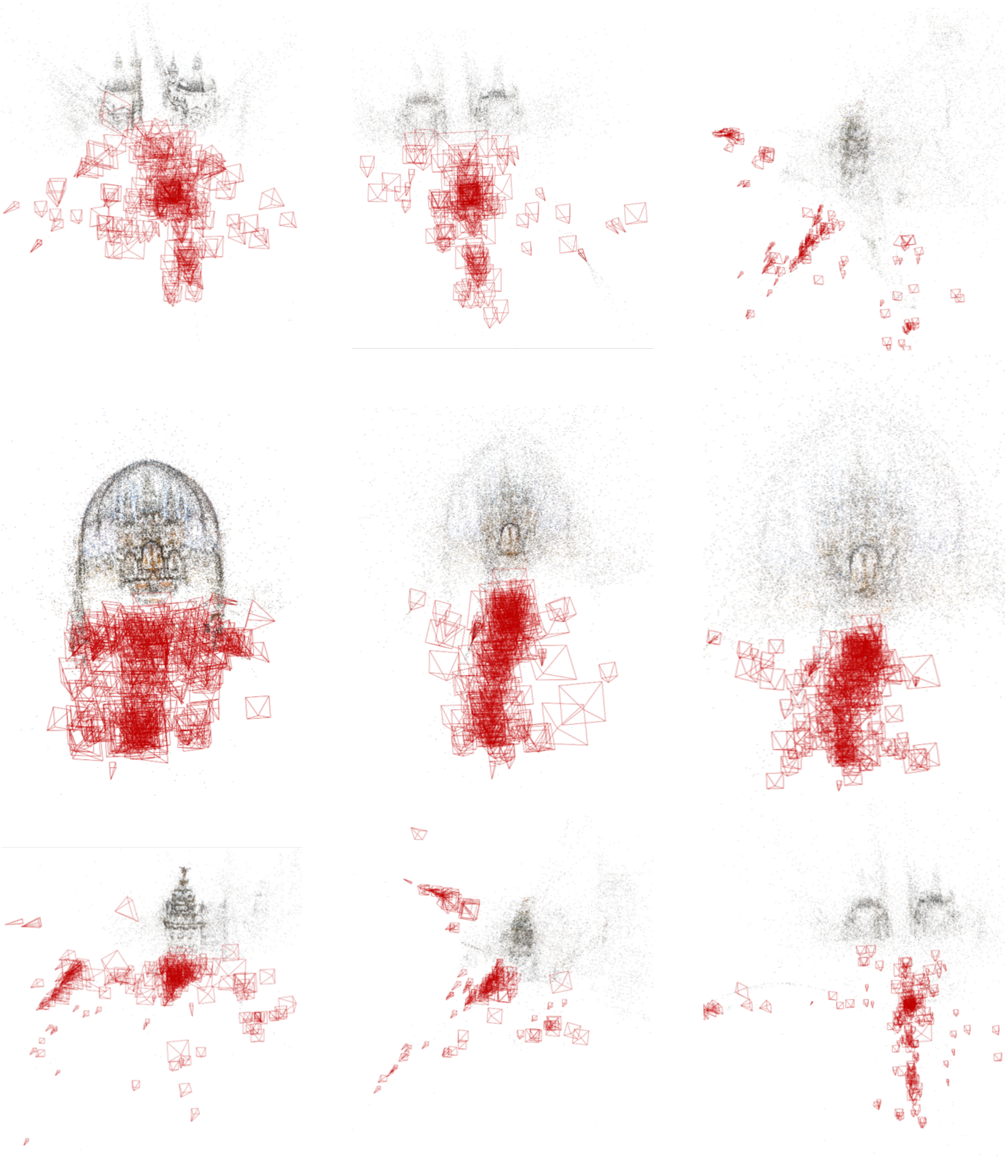

(a) Our recovery (b) ESFM recovery (c) GASFM recovery

Figure 3: **Reconstruction results on scenes from the 1DSFM dataset.** The figure shows 3D reconstructions and camera pose estimation. The triplet in each row shows reconstruction with our method (left), ESFM (Moran et al., 2021) (middle), and GASFM (Brynte et al., 2023) (right). The scenes are Piazza del Popolo (top row, 33.1% outliers), Montreal Notre Dame (middle row, 33% outliers), and Madrid Metropolis (bottom row, 39.4% outliers).

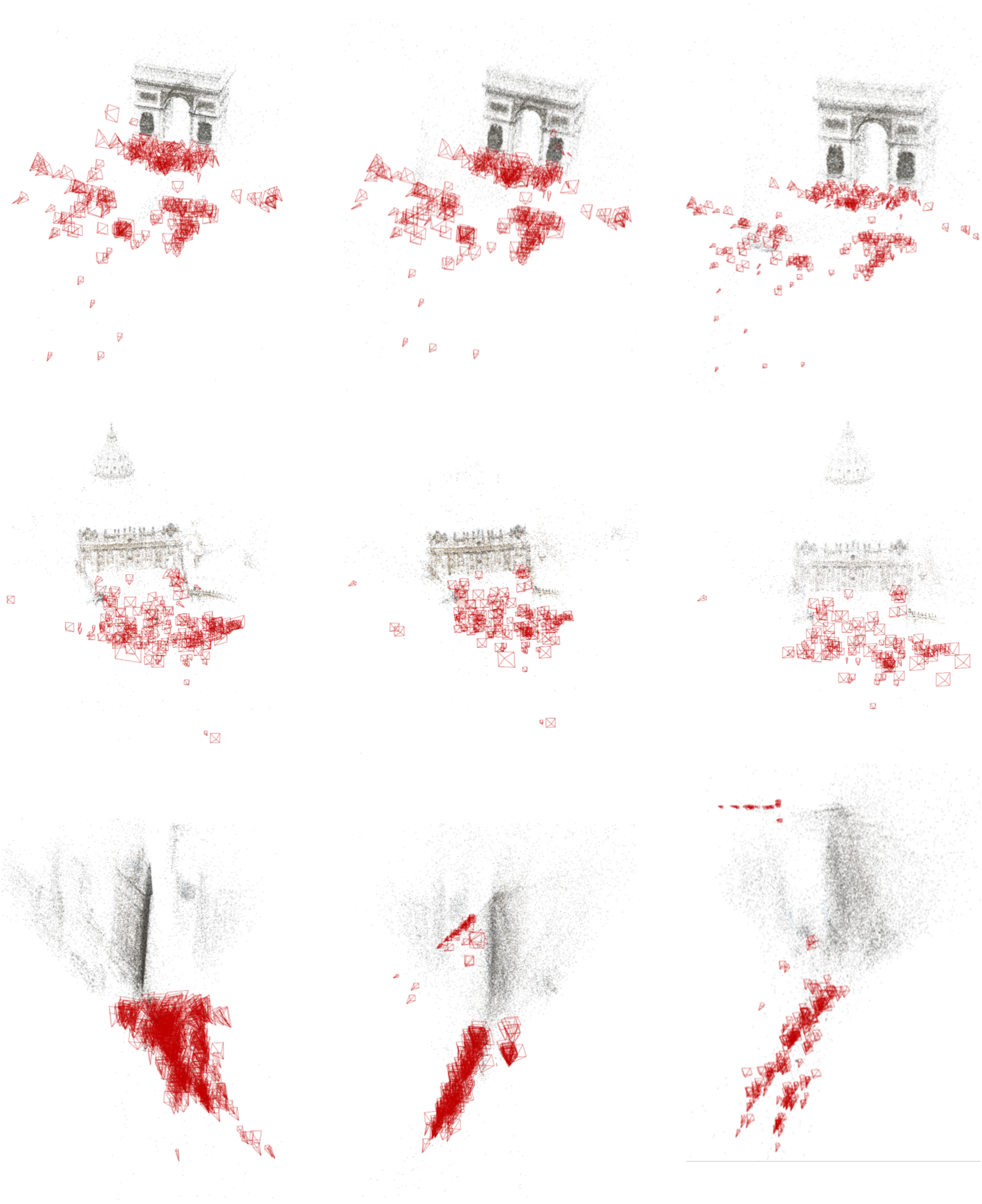

(a) Our recovery

(b) ESFM recovery

(c) GASFM recovery

Figure 4: **Reconstruction results on scenes from MegaDepth dataset.** The figure shows 3D reconstructions and camera pose estimation. The triplet in each row shows reconstruction with our method (left), ESFM (Moran et al., 2021) (middle), and GASFM (Brynte et al., 2023) (right). The scenes are 0012 (top row, 16.3% outliers), 0015 (middle row, 20.6% outliers), and 0060 (bottom row, 41.6% outliers).

B IMPLEMENTATION DETAILS

Our code and preprocessed point tracks data will be made publicly available.

Framework. Our method was trained and evaluated on NVIDIA A40 GPUs (48GB of GPU Memory). We used PyTorch (Paszke et al., 2019) as the deep learning framework and the ADAM optimizer (Kingma & Ba, 2014) with normalized gradients.

Training. During training, for each epoch, we processed all training scenes sequentially. For each scene, we randomly selected a subset of 10%-20% of the images in the scene. We used a validation set for early stopping. The validation and test sets were evaluated by using the complete point tracks matrix. The training time of our model on the Megadepth dataset took roughly 16 hours on a single NVIDIA A40 GPU. We fix the seed to 20.

Architecture details. We use normalized point tracks $\mathbf{x}_{ij}$, as inputs to our method which are normalized using the known intrinsic parameters. The shared features encoder E has 3 layers, each with 256 feature channels and ReLU activation. The camera head H_{cams}, 3D point head H_{pts}, and the outliers classification head H_{outlier}, each have 3 layers with 256 channels. After each layer in E we normalize its features by subtracting their mean.

Hyper-parameter search. We tried different implementation hyper-parameters including (1) learning rates $\in \{1e-2, 1e-3, 1e-4\}$, (2) network width $\in \{128, 256, 512\}$ for the encoder E and the heads, (3) number of layers $\in \{2, 3, 4, 5\}$ in these networks, and (4) threshold for outlier removal $\in \{0.4, 0.5, 0.6, 0.7, 0.8\}$. For the Strecha and BlendedMVS datasets, we chose a threshold of 0.8, as these datasets are captured with a single camera and therefore contain fewer outliers.

Bundle adjustment For the bundle adjustment, we employed the Ceres Solver's implementation of bundle adjustment Agarwal et al. with the Huber loss to enhance robustness (with parameter 0.1). In each bundle adjustment round, we limited the number of iterations to 300 or until convergence, whichever occurred first.

C CONSTRUCTING POINT TRACKS

Our preprocessing step for constructing the point tracks is as follows:

1. Extracting SIFT (Lowe, 2004) features for all the images.
2. Applying exhaustive pair-wise RANSAC (Fischler & Bolles, 1981) matching for all image pairs.
3. Chaining each sequence of two-view matches for creating a point track.

We discard a 3D point and its track if it is viewed in less than 3 cameras or if it includes an inconsistent cycle, i.e., we detect two key points in the same image for the same point track.

The above preprocess defines a valid point track structure for our architecture. We next define the inliers/outliers labeling process, which assumes that every training scene has an associated COLMAP (Schönberger & Frahm, 2016) reconstruction:

1. For each track within our point track set:
   (a) Identify the corresponding track in COLMAP's reconstruction output
   (b) For every keypoint in the track:
      - Label the keypoint as an outlier if it does not appear in the corresponding COLMAP track; otherwise, label it as an inlier.
2. Remove keypoints labeled as outliers from the point tracks.
3. Triangulate the 3D points from the cleaned point tracks using the ground truth camera poses obtained from COLMAP.
4. Calculate the reprojection error for the triangulated 3D points across the entire point tracks, including the ones labeled initially as outliers.
5. Assign an inlier label to each keypoint whose reprojection error is below 4 pixels; keypoints exceeding this threshold are classified as outliers.

D Additional Results

Here we show median results for the MegaDepth and 1DSFM experiments (Tables 9 and 10). We further validate the importance of our Robust BA compared to a standard BA (Table 11).

Table 9: MegaDepth experiment. The table shows the **median** values of the rotation (in degrees) and translation errors. (Above the middle rule are Group 1 scenes with <1000 images; below are Group 2 scenes with >1000 images, subsampled to 300 for testing.) Winning results are marked in bold and underlined. Yellow represents the best result among the deep-based algorithms, and green among the classical algorithms.

Scene	N_c	Outliers%	**Ours**			ESFM			GASFM			Theia			GLOMAP			ESFM*		
			N_r	Rot	Trans	N_r	Rot	Trans	N_r	Rot	Trans	N_r	Rot	Trans	N_r	Rot	Trans	N_r	Rot	Trans
0238	522	44.6	283	0.72	**0.043**	76	1.75	0.100	76	5.15	0.323	**506**	0.54	0.109	499	**0.22**	**0.043**	512	0.64	0.038
0060	528	41.6	503	0.14	**0.011**	303	8.54	1.268	258	13.81	2.744	**525**	0.26	0.039	522	**0.04**	0.012	524	0.02	0.003
0197	870	40.7	667	2.06	0.133	281	4.14	0.183	454	6.65	0.688	**855**	0.77	0.118	814	**0.13**	**0.016**	825	0.11	0.008
0094	763	40.1	537	0.38	**0.015**	93	17.62	2.048	359	0.88	0.028	**742**	0.21	0.033	717	**0.20**	1.957	643	0.18	0.014
0265	571	38.8	346	**0.74**	**0.209**	270	14.64	1.666	274	18.91	1.716	554	4.11	1.651	**558**	6.66	1.889	559	0.06	0.022
0083	635	31.3	596	0.15	0.009	568	0.90	0.027	574	2.48	0.099	**632**	0.15	0.013	614	**0.04**	**0.007**	556	16.03	0.973
0076	558	30.5	524	0.11	0.010	454	1.60	0.091	431	**0.05**	**0.006**	**549**	0.44	0.058	541	0.08	0.017	547	0.03	0.004
0185	368	30.0	350	**0.04**	**0.006**	261	0.53	0.037	254	0.46	0.048	**365**	0.31	0.037	**365**	0.11	0.012	130	29.39	2.160
0048	512	24.2	474	2.16	0.098	469	1.57	0.080	481	0.60	0.028	**507**	0.21	0.020	506	**0.06**	**0.007**	508	0.05	0.002
0024	356	23.0	309	0.58	0.046	271	4.64	0.187	300	0.48	0.104	**355**	0.24	0.091	339	**0.07**	**0.045**	343	1.41	0.078
0223	214	17.0	204	1.56	0.078	191	1.81	0.180	194	1.53	1.106	212	0.89	0.152	**214**	**0.41**	**0.046**	211	0.06	0.010
5016	28	0.2	**28**	0.10	0.005	**28**	0.07	0.004	**28**	0.06	**0.003**	**28**	0.07	0.019	**28**	**0.04**	0.016	28	0.02	0.003
0046	440	14.6	399	0.78	0.028	97	0.58	0.017	426	0.35	0.011	434	0.16	0.016	**440**	**0.02**	**0.002**	33	29.18	1.331
0099	299	47.4	190	3.18	0.697	104	2.21	0.402	128	3.95	0.409	**297**	1.79	0.394	255	**0.06**	**0.026**	243	2.97	0.618
1001	285	43.9	251	**1.41**	**0.276**	241	2.44	0.860	261	2.26	0.386	276	4.85	2.893	**281**	3.29	2.645	280	0.08	0.053
0231	296	42.2	246	0.38	0.014	214	0.28	0.011	209	**0.19**	**0.009**	**286**	0.58	0.072	279	0.20	0.021	284	0.26	0.011
0411	299	29.9	273	**0.07**	**0.009**	188	6.21	0.338	232	1.28	0.051	**293**	0.19	0.079	269	0.09	0.036	288	0.05	0.007
0377	295	27.5	210	0.28	0.014	162	0.25	0.010	167	**0.09**	**0.008**	**269**	0.29	0.075	268	0.23	0.021	279	0.52	0.022
0102	299	25.8	284	0.07	**0.007**	255	0.50	0.032	278	0.37	0.023	**294**	1.03	0.114	293	**0.04**	0.013	155	13.56	2.859
0147	298	24.6	207	2.07	0.088	197	2.05	0.097	225	5.26	0.296	284	**1.10**	**0.064**	**290**	1.78	2.056	251	1.14	0.041
0148	287	24.6	197	**0.54**	**0.024**	206	0.59	0.028	209	0.59	0.028	275	3.01	0.301	**283**	3.09	1.301	249	0.46	0.023
0446	298	22.1	288	0.41	0.013	283	0.70	0.021	291	0.20	**0.008**	289	0.61	0.073	**296**	**0.14**	0.020	294	0.22	0.006
0022	297	21.2	274	0.13	**0.011**	241	0.51	0.025	263	0.16	0.013	**296**	0.28	0.065	281	**0.08**	0.023	289	0.08	0.008
0327	298	21.0	271	0.11	**0.006**	281	0.75	0.022	284	**0.10**	0.007	288	0.73	0.087	**290**	7.14	0.333	294	0.03	0.003
0015	284	20.6	215	0.27	0.021	142	1.30	0.105	149	6.35	0.556	244	0.42	0.084	**274**	**0.11**	**0.014**	185	0.43	0.053
0455	298	19.8	293	0.18	**0.010**	293	0.23	0.014	294	0.29	0.016	294	0.36	0.047	**298**	**0.14**	0.017	298	0.26	0.012
0496	297	19.2	281	**0.13**	**0.006**	281	2.81	0.197	277	0.44	0.027	285	0.61	0.080	**291**	0.16	0.028	293	0.23	0.009
1589	299	17.4	290	0.08	**0.003**	284	0.40	0.008	283	1.00	0.016	288	0.32	0.057	**299**	**0.03**	0.007	296	0.20	0.004
0012	299	16.3	287	0.39	0.023	291	2.04	0.131	294	0.21	0.018	129	0.56	0.092	**295**	**0.20**	**0.017**	294	0.22	0.013
0104	284	16.2	193	**0.16**	**0.009**	220	11.31	0.568	228	1.32	0.051	265	9.24	0.658	**280**	9.86	0.550	200	0.49	0.019
0019	299	15.4	250	**0.04**	**0.004**	267	2.46	0.128	293	0.58	0.023	271	0.31	0.030	**296**	**0.04**	**0.004**	296	2.23	0.097
0063	293	14.5	262	0.26	**0.013**	262	1.18	0.057	257	0.40	0.020	268	0.45	0.063	**288**	**0.17**	0.017	275	0.15	0.009
0130	285	14.4	192	**0.10**	**0.005**	192	0.94	0.030	194	1.00	0.033	187	0.63	0.072	**281**	0.94	0.535	282	0.82	0.041
0080	284	12.9	139	**0.27**	**0.010**	137	0.32	0.012	139	1.36	0.054	278	1.84	0.335	**283**	1.71	0.169	163	0.32	0.011
0240	298	11.9	275	1.56	0.090	274	1.14	0.064	272	2.00	0.113	278	0.47	0.057	**294**	**0.17**	**0.041**	296	0.09	0.006
0007	290	11.7	172	0.23	0.010	260	25.50	1.432	280	0.18	0.010	277	0.69	0.071	**290**	**0.06**	**0.006**	286	0.96	0.053
Mean	379	25.6	298	**0.61**	**0.057**	239	3.46	0.291	267	2.25	0.252	346	1.08	0.228	353	1.05	0.332	319	2.86	0.240

Table 10: 1DSFM experiment. The table shows the **median** values of the rotation (in degrees), and translation errors. Winning results are marked in bold and underlined. Yellow represents the best result among the deep-based algorithms and green among the classical algorithms.

Scene	N_c	Outliers%	**Ours**			ESFM			GASFM			Theia			GLOMAP			ESFM*		
			N_r	Rot	Trans	N_r	Rot	Trans	N_r	Rot	Trans	N_r	Rot	Trans	N_r	Rot	Trans	N_r	Rot	Trans
Alamo	573	32.6	484	0.97	**0.037**	457	1.00	0.047	448	2.64	0.115	553	2.29	0.539	**557**	**0.61**	0.144	526	0.35	0.016
Ellis Island	227	25.1	214	**0.32**	**0.036**	196	18.88	1.554	198	19.24	1.548	213	3.85	0.712	**219**	0.46	0.087	220	0.19	0.026
Madrid Metropolis	333	39.4	244	4.42	0.193	151	19.85	1.641	159	21.76	1.560	-	-	-	**320**	**0.53**	**0.096**	290	23.71	2.154
Montreal Notre Dame	448	31.7	346	1.00	**0.056**	309	4.42	0.790	311	4.83	0.945	422	2.63	0.808	**444**	**0.40**	0.158	414	0.07	0.009
Notre Dame	549	35.6	517	0.55	**0.025**	487	**0.43**	**0.025**	499	0.51	**0.025**	314	1.54	0.133	**543**	1.15	0.130	528	0.30	0.012
NYC Library	330	33.6	224	1.48	**0.074**	177	1.93	0.102	218	3.74	0.264	**534**	1.65	0.360	323	**0.46**	0.075	301	1.16	0.087
Piazza del Popolo	336	33.1	249	0.80	**0.034**	204	3.20	0.353	198	3.79	0.583	325	1.15	0.342	**331**	**0.28**	0.084	303	0.88	0.052
Tower of London	467	27.0	94	0.48	**0.012**	196	13.59	0.564	152	33.19	2.339	448	3.23	0.527	**466**	**0.42**	0.071	213	4.53	0.163
Vienna Cathedral	824	31.4	479	**0.48**	**0.016**	551	1.40	0.046	558	1.67	0.044	772	9.32	0.838	**822**	0.61	0.206	536	0.44	0.013
Yorkminster	432	29.0	331	4.67	0.299	215	6.15	0.302	251	7.80	0.378	390	4.26	0.948	**418**	**0.60**	**0.069**	389	6.48	0.265

Table 11: **Bundle-Adjustment (BA) ablation.** We compare the effect of post-processing with a robust vs. standard BA. For each scene, we show the number of input images (denoted N_c) and the fraction of outliers. For each model, we show the number of images used for reconstruction (denoted N_r) and the mean values of the rotation (in degrees) and translation errors.

Scene	N_c	Outliers%	Robust BA (Ours)			Standard BA)		
			N_r	Rot	Trans	N_r	Rot	Trans
Alamo	573	32.6	484	**3.66**	**0.515**	**568**	10.18	1.970
Ellis Island	227	25.1	214	**0.82**	**0.122**	**227**	4.05	1.045
Madrid Metropolis	333	39.4	244	**8.42**	**0.827**	**333**	20.07	2.352
Montreal Notre Dame	448	31.7	346	**2.82**	**0.352**	**447**	4.52	0.563
Notre Dame	549	35.6	517	**1.20**	**0.231**	**548**	3.45	0.378
NYC Library	330	33.6	224	**3.96**	**0.429**	**329**	24.94	3.571
Piazza del Popolo	336	33.1	249	**2.20**	**0.186**	**335**	21.68	2.001
Tower of London	467	27.0	94	**0.67**	**0.026**	**465**	57.41	3.347
Vienna Cathedral	824	31.4	479	**1.52**	**0.112**	**819**	43.38	2.784
Yorkminster	432	29.0	331	**14.54**	**1.468**	**431**	21.17	3.660